Remote Sensing Image Stripe Noise Removal: From Image Decomposition Perspective

Yi Chang, *Student Member, IEEE*, Luxin Yan, *Member, IEEE*, Tao Wu, and Sheng Zhong

Abstract—Stripe noise removal (destriping) is a fundamental problem in remote sensing image processing that holds significant practical importance for subsequent applications. These variational destriping methods have obtained impressive results and attracted widely studied research interests. However, most of them are dedicated to estimate the clear image from the striped one, paying much attention to the image itself, while ignoring the structural characteristic of stripe, which would easily cause damages to the image structure and leave residual stripes in image recovery. In this paper, we treat the image and stripe components equally and convert the image destriping task as an image decomposition problem naturally. We first give a detailed analysis about the structural characteristic of stripes and the prior knowledge about the remote sensing images. Then, incorporating them, we propose a low-rank-based single-image decomposition model (LRSID) to separate the original image from the stripe component perfectly. This low-rank constraint for the stripe perfectly matches the fact that only parts of data vectors are corrupted but the others are not. Moreover, we further utilize the spectral information of the remote sensing images, and we extend our 2-D image decomposition method to the 3-D case. Extensive experiments on both simulated and real data have been carried out to validate the effectiveness and efficiency of the proposed algorithms.

Index Terms—Decomposition, image destriping, low rank, remotely sensed image, total variational (TV).

I. INTRODUCTION

REMOTE sensing imagery has played an important role in various applications, including earth climate, agriculture, and military [1]–[3]. However, there in practice always exist various kinds of stripe noise in different remote sensing imaging systems, including push-broom [4] and cross-track imaging devices [5], mainly due to the differences in the response of detectors, calibration error, and so on. The stripes in remote sensing images not only sharply degrade the image quality in the visual effect but also risk their suitability for subsequent processing, e.g., image unmixing [6] and classification [7]. The goal of our work is to remove the stripes and improve image quality before the subsequent interpretation.

In the past decades, the stripe removal problem has attracted many research interests, and the destriping methods can be
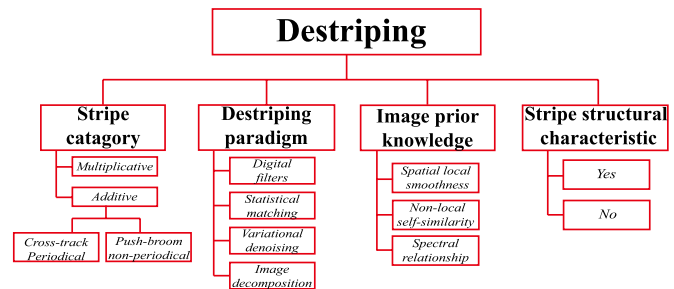
Fig. 1. Key properties of destriping algorithms.

categorized from different viewpoints, as shown in Fig. 1. From the viewpoints of methodology, available destriping methods can be mainly classified into three categories. The filtering-based methods are widely used due to their simplicity [8]–[10]. One limitation of this kind of method is the poor destriping capacity since they hold the assumption that stripes are periodic and can be identified from the power spectrum. The image structures with the same frequencies as stripes will also be affected along the filtering procedure. Because the stripes only affect partial columns or rows in images and leave the others intact, the second category methods utilize the statistical property of digital numbers of the fine detectors. The main idea of these methods is to rectify the distribution of the stripes to a reference distribution [11]–[14]. However, their performances are highly limited because the strong similarity assumptions [13] are always invalid.

During the past few years, some variational destriping methods regard stripe removal issue as an ill-posed inverse problem, and these methods have made significant progress [15]–[22]. The basic idea is that the clear image can be well constrained via some regularization terms, so as to be estimated from the striped image. In [15], Shen and Zhang first proposed the Huber–Markov variational model to remove the stripes with spatially local adaptive edge-preserving ability. The authors in [16] proposed a sophisticated unidirectional variational model (UTV) for single-image destriping and made use of the structural and directional characteristic of the stripes with better detail-preserving performance. We have extended the UTV model into the multispectral case [18]. Recently, the low-rank prior-based destriping methods have been introduced by Lu *et al.* [20] and Zhang *et al.* [21]. By stacking the multispectral images into a 2-D matrix, they exploited the inherently low-dimensional characteristic of the multispectral data and recovered the low-rank matrix, to remove all outliers, including stripes, from the striped data.
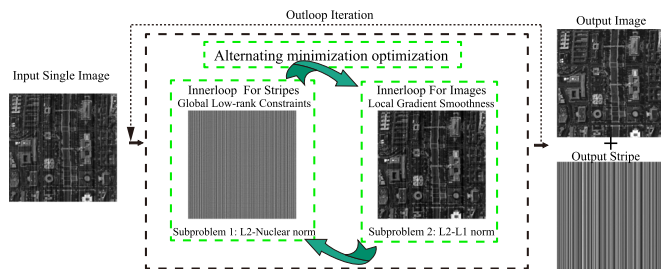
Fig. 2. Illustration of our image decomposition model for destriping.

Although the variation-based methods mentioned earlier have achieved encouraging destriping performance, they still face some problems when dealing with various kinds of stripes. Most of them focus on various properties of the image, such as gradient-domain smoothness [16], sparsity in dictionary coefficient domain [18], and low rank [20], [23], [24], whereas few of them take into account the characteristic of the stripe; hence, many image details may be removed along with stripes. Recently, some interesting works have stepped toward the opposite direction by estimating the stripe component [4], [17], [25]. However, they focus on estimating the stripe component, while less taking the image prior into consideration. In this paper, we address the aforementioned concerns from an image decomposition perspective. We give a detailed analysis on both the structural characteristics of the image and the stripes, and we treat the destriping issue as an image decomposition problem, in which the low-rank prior is introduced to naturally characterize the subspace spanned by the stripes, interpreting the stripes component to be low rank, whereas the image component is leveraged by total variation (TV), as shown in Fig. 2. In this framework, the degraded image is decomposed into the stripe component and the image component, in which these two components are treated equally and decoupled completely.

Compared with state-of-the-art low-rank destriping methods, the advantages of our decomposition method are twofold. First, previous methods introduce the low-rank constraint on the man-made 2-D matrix stacked by multiple bands, which may fail unexpectedly when the bands' similarity cannot be guaranteed, whereas our method could directly apply on the single-band image. Note that our image-decomposition-based method could also be easily extended to a multispectral case (we will discuss this extension in Section IV). Second, the traditional low-rank matrix recovery model is designed for the small structure noise removal problem [26], which is captured by the L_1-norm (sum of all the elements). While for stripes with an obvious directional characteristic and a large area, the low-rank induced nuclear norm is more appropriate than the L_1-norm (we will analyze this in Section II-B).

Contribution: Extensive experimental results on different multidetector images verify the effectiveness and efficiency of the proposed method. Our contributions are threefold.

1) We convert the destriping issue into an image decomposition problem and propose a low-rank matrix decomposition model to remove various kinds of stripes, which offers a new perspective to the image destriping task.

2) The directional characteristic of the stripe is analyzed in detail, and we propose a decomposition model with low-

rank prior characterizing the subspace spanned by the stripe, which separates the image structure from the stripe naturally.

3) The proposed destriping method is based on a single image, and this is also extended to the multispectral case, which makes the proposed model more robust and effective to various stripes.

The remainder of this paper is organized as follows. In Section II, the common characteristic of stripe noise is analyzed in detail. The image decomposition model and its optimizations are formulated in Section III. Section IV dedicates to the multispectral extension of our method. Experimental results and discussion are reported in Section V. Finally, we conclude the paper in Section VI, with a discussion on promising directions for future research.

II. STRIPE NOISE AND IMAGE CHARACTERISTIC ANALYSIS

A. Image Observation Model

For remote sensing images, the stripes are mainly due to both additive and multiplicative components [15]. The stripes caused by the multiplicative component can be well calibrated online [27], [28]. Moreover, a well-designed additive model can be applied to the multiplicative case by only introducing the logarithm as in [4]. In this paper, we mainly focus on the additive stripe noise. Mathematically, the degradation model can be formulated as [21]

$$\boldsymbol{Y} = \boldsymbol{X} + \boldsymbol{B} + \boldsymbol{N} \tag{1}$$

where $\boldsymbol{Y} \in \mathbb{R}^{R \times C}$ is the measured image; R and C stand for the number of the rows and columns, respectively; $\boldsymbol{X}$ is the desired clear image; $\boldsymbol{B}$ is the offset also named as additive stripe component; and $\boldsymbol{N}$ is Gaussian white noise. The goal of our work is to estimate both the clear image and the stripe simultaneously from the degraded image.

B. Directional Characteristic and Low-Rank Prior of Stripes

Compared with Gaussian noise, the stripe noise has a significantly structural characteristic, exhibiting a noteworthily directional characteristic. *Different from a traditional random noise removal problem, how to utilize these properties is the key point in the destriping task.* Münch *et al.* [9] and Pande-Chhetri and Abd-Elrahman [10] proposed the wavelet decomposition to extract the directional components induced by stripes, as shown in Fig. 3, and only filter on these specific components. We can observe that, after wavelet decomposition, the induced components by stripes only exist in the vertical direction, as shown in Fig. 3(d).

Moreover, we quantitatively analyze the property of stripes in remote sensing images. We use the wavelet-based destriping method [10] to remove both the periodical stripes in MODIS images and the nonperiodical stripes in hyperspectral images, as shown in Fig. 4. Interestingly, we found that the ranks of both stripe matrices are 1. That is to say, the subspace spanned by the additive stripes can be well represented by the low-rank constraint.
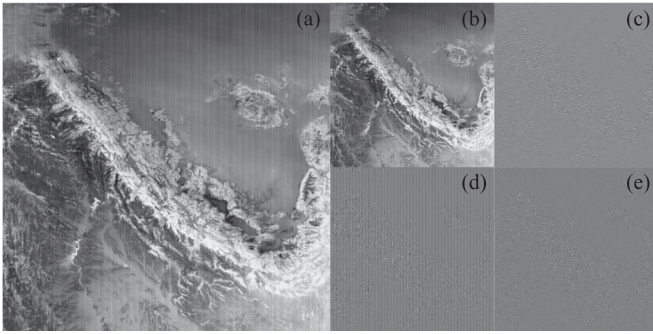
Fig. 3. Wavelet decomposition results. The induced components by stripes only exist in the vertical direction.
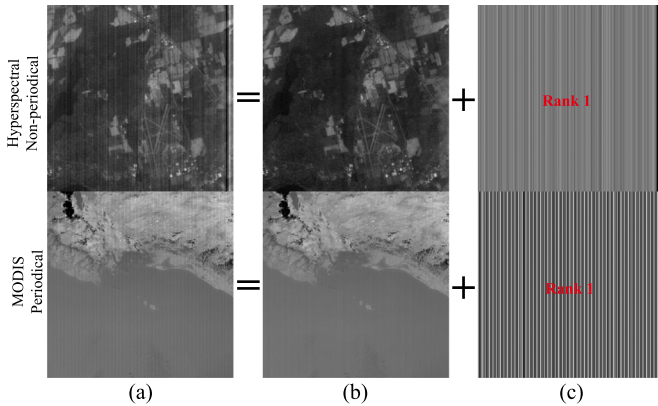

Fig. 4. Low-rank property of various stripes in remote sensing images. (a) Degraded images. (b) Clear image component. (c) Stripe component.
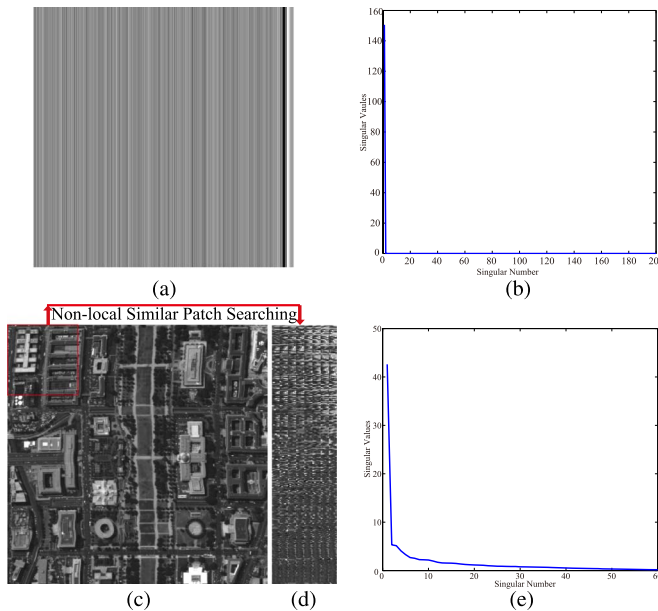

Fig. 5. Low-rank comparison between stripe and man-made matrix. (a) Stripe. (b) Singular values of (a). (c) Hyperspectral image. (d) Man-made low-rank matrix from (c). (e) Singular values of (d).

Furthermore, we compared the ranks of the stripes and the man-made low-rank matrix stacked by nonlocal similarity patches [21], as shown in Fig. 5. Fig. 5(a) shows a striped image, and Fig. 5(d) shows the man-made low-rank matrix formed by nonlocal similarity patches in the red square of Fig. 5(c). The singular values of the corresponding images are shown in

Fig. 5(b) and (e), from which we can observe that the singular values of striped image rapidly decrease to zero with rank 1, whereas the singular values of the man-made image slowly decrease to zero with rank 60. This phenomenon demonstrates that the rank of the natural image or man-made matrix [20]–[22] is absolutely higher than that of the stripes. Therefore, we propose to use the low-rank constraint on the stripe directly and not on the image. Our low-rank constraint is in line with [4]. The authors [4] implicitly accounted for an exact rank-1 model for the stripe. Our method will cover the solution of [4], and this can be applied to much more complex and real non-rank-1 stripe situations. This flexibility makes our method more robust to stripe of various remote sensing imaging systems.

C. Knowledge About Remote Sensing Images

The auxiliary information for remote sensing images can be divided into three main categories: spatial local sparsity, spatial nonlocal self-similarity, and spectral correlation, as shown in Fig. 1. The spatial local sparsity priors include the gradient-smoothness-based TV [29] and Huber–Markov prior [30], the transformed-domain sparsity-based framelet [31] and dictionary learning [32]. The spatial nonlocal self-similarity can be utilized via low-rank prior [33] or group sparsity [34]. The spectral correlation is also used in various manners, such as low-rank prior [35] and spectral TV [19]. The effect of each category information about the remote sensing images has been discussed thoroughly in these works. On the contrary to most of the previous works, we argue that the success of a good destriping algorithm is mainly owing to the utilization of structural characteristic of the stripe, not on the image. Therefore, in this work, we only choose the conventional anisotropic TV as our image prior. It is reasonable for us using anisotropic TV to enforce more constraint across the stripe line direction (horizontal gradient), while less constraint along the stripe line direction (vertical gradient).

III. PROPOSED SINGLE-IMAGE LOW-RANK DECOMPOSITION MODEL

Here, we will give our Low-Rank Single-Image Decomposition (LRSID) model and its optimization. Although there are several low-rank-based striping works [20]–[22], they all treat the destriping task as the grossly corrupted error removal problem and make use of the robust principal component analysis model [33], which only focuses on the characteristic of images to estimate the clear image. However, the stripes have an obvious directional property, which is worth taking into consideration along with the image content, and thus help decouple the image and stripe components more completely. Thus, in this work, we propose an image decomposition strategy for the destriping problem to model both the characteristics of stripe and image components, simultaneously.

A. Single-Image Low-Rank Decomposition

For the image decomposition problem, the general model can be formulated as

$$\min_{\boldsymbol{X},\boldsymbol{B}} \frac{1}{2}\|\boldsymbol{X} + \boldsymbol{B} - \boldsymbol{Y}\|_F^2 + \tau P(\boldsymbol{X}) + \lambda P(\boldsymbol{B}). \qquad (2)$$

As we have analyzed before, the stripe component is a global and well-patterned repeated structure with an extremely small rank, which motivates us naturally to use the low-rank constraint for the stripe component. As for the image, we introduce the widely used TV regularization [29], due to its desirable properties, such as convexity, the ability to preserve sharp edges, and ease to be implemented. Thus, the formulation of our image decomposition model is given by

$$\min_{\boldsymbol{X},\boldsymbol{B}} \frac{1}{2}\|\boldsymbol{X}+\boldsymbol{B}-\boldsymbol{Y}\|_F^2 + \tau\|\boldsymbol{X}\|_{\text{TV}} + \lambda\text{rank}(\boldsymbol{B}) \quad (3)$$

where $\|\boldsymbol{X}\|_{\text{TV}} = \sum_i(|(\nabla\boldsymbol{X})_i|)$, and $\nabla = (\nabla_x; \nabla_y)$ denotes the horizontal and vertical derivative operators at pixel i, respectively. Because of the nonconvexity of the rank constraint, we introduce the nuclear norm to replace it as its convex surrogate functional [36], as follows:

$$\min_{\boldsymbol{X},\boldsymbol{B}} \frac{1}{2}\|\boldsymbol{X}+\boldsymbol{B}-\boldsymbol{Y}\|_F^2 + \tau\|\boldsymbol{X}\|_{\text{TV}} + \lambda\|\boldsymbol{B}\|_*. \quad (4)$$

According to [37], under suitable conditions, the rank minimization program (3) and the convex nuclear norm (4) are formally equivalent in the sense that they have exactly the same unique solution. In our experimental results, we have also found that the rank of the restored stripe via (4) is exactly the same as the given rank in (3). Our final model (4) is very simple and easy to understand, in which the main structures of the image are leveraged via the TV regularization term, whereas the stripes are well depicted by the nuclear norm, so that the two components can be decoupled perfectly. The proposed decomposition model aims to optimize two variables simultaneously, which can be solved via an alternatively minimizing strategy. Thus, the optimization problem of (4) becomes two convex subproblems: an L_1-regularized and a nuclear-norm-regularized least square problem. As for the alternative direction multiplier method (ADMM) [38] algorithm to solve problem (4), the TV is strictly convex and has a Lipschitz continuous gradient with only one block. In such a situation, the convergence property of a generalized ADMM can be well guaranteed with proper penalty parameters [39]. By choosing a proper initialization and regularization parameters, we can always obtain a satisfactory result.

B. Optimization

1) Stripe Update: Given image $\boldsymbol{X}$, the stripe $\boldsymbol{B}$ can be estimated from the following minimization problem:

$$\hat{\boldsymbol{B}} = \arg\min_{\boldsymbol{B}} \frac{1}{2}\|\boldsymbol{X}+\boldsymbol{B}-\boldsymbol{Y}\|_F^2 + \lambda\|\boldsymbol{B}\|_*. \quad (5)$$

Equation (5) is a typical low-rank matrix approximation problem which has a closed-form solution and can be easily solved by a soft-thresholding operation on the singular values of observation matrix [40], as follows:

$$\begin{cases} \boldsymbol{B}^{k+1} = \boldsymbol{U}\left(\text{shrink\_}L_*(\Sigma, \lambda)\right)\boldsymbol{V}^T \\ \text{shrink\_}L_*(\Sigma, \lambda) = \text{diag}\left\{\max(\Sigma_{ii} - \lambda, 0)\right\}_i \end{cases} \quad (6)$$

where $\boldsymbol{Y} - \boldsymbol{X} = \boldsymbol{U}\Sigma\boldsymbol{V}^T$ is the singular-value decomposition of $\boldsymbol{Y} - \boldsymbol{X}^k$, and Σ_{ii} is the diagonal element of the singular-value matrix Σ.

2) Image Update: Given stripe $\boldsymbol{B}$, the image $\boldsymbol{X}$ can be estimated from the following minimization problem:

$$\hat{\boldsymbol{X}} = \arg\min_{\boldsymbol{X}} \frac{1}{2}\|\boldsymbol{X}+\boldsymbol{B}-\boldsymbol{Y}\|_F^2 + \tau_x\|\nabla_x\boldsymbol{X}\|_1 + \tau_y\|\nabla_y\boldsymbol{X}\|_1 \quad (7)$$

where $\|\cdot\|_1$ denotes the sum of absolute value of the matrix elements. Since the stripe exhibits a significant directional pattern, it is natural for us to account for a different weight τ for the spatial $\nabla_x\boldsymbol{X}$ and $\nabla_y\boldsymbol{X}$ difference. For simplicity, we still use the same τ in the next formula derivation but different values in real implementation. Due to the nondifferentiability of the L_1-norm, we introduce the ADMM [38] to convert the original problem into two easy subproblems with closed-form solutions. By introducing two auxiliary variables $\boldsymbol{D}_x = \nabla_x\boldsymbol{X}$ and $\boldsymbol{D}_y = \nabla_y\boldsymbol{X}$, (7) is equivalent to the following problem:

$$\begin{aligned} \{\hat{\boldsymbol{X}}, \hat{\boldsymbol{D}}_x, \hat{\boldsymbol{D}}_y\} = \arg\min_{\boldsymbol{X},\boldsymbol{D}_x,\boldsymbol{D}_y} &\frac{1}{2}\|\boldsymbol{X}+\boldsymbol{B}-\boldsymbol{Y}\|_F^2 \\ &+ \tau\|\boldsymbol{D}_x\|_1 + \tau\|\boldsymbol{D}_y\|_1 \\ &+ \frac{\alpha}{2}\left\|\boldsymbol{D}_x - \nabla_x\boldsymbol{X} - \frac{\boldsymbol{J}_x}{\alpha}\right\|_F^2 \\ &+ \frac{\alpha}{2}\left\|\boldsymbol{D}_y - \nabla_y\boldsymbol{X} - \frac{\boldsymbol{J}_y}{\alpha}\right\|_F^2 \end{aligned} \quad (8)$$

where $\boldsymbol{J}_x$ and $\boldsymbol{J}_y$ are the Lagrangian multipliers, and α is a positive scalar. Equation (8) can be written as

$$\begin{aligned} \{\hat{\boldsymbol{X}}, \hat{\boldsymbol{D}}\} = \arg\min_{\boldsymbol{X},\boldsymbol{D}} &\frac{1}{2}\|\boldsymbol{X}+\boldsymbol{B}-\boldsymbol{Y}\|_F^2 + \tau\|\boldsymbol{D}\|_1 \\ &+ \frac{\alpha}{2}\left\|\boldsymbol{D} - \nabla\boldsymbol{X} - \frac{\boldsymbol{J}}{\alpha}\right\|_F^2 \end{aligned} \quad (9)$$

by letting

$$\boldsymbol{D} = \begin{bmatrix} \boldsymbol{D}_x \\ \boldsymbol{D}_y \end{bmatrix}, \quad \nabla = \begin{bmatrix} \nabla_x \\ \nabla_y \end{bmatrix}, \quad \boldsymbol{J} = \begin{bmatrix} \boldsymbol{J}_x \\ \boldsymbol{J}_y \end{bmatrix}. \quad (10)$$

The $\boldsymbol{X}$-related subproblem is given by

$$\hat{\boldsymbol{X}} = \arg\min_{\boldsymbol{X}} \frac{1}{2}\|\boldsymbol{X}+\boldsymbol{B}-\boldsymbol{Y}\|_F^2 + \frac{\alpha}{2}\left\|\boldsymbol{D} - \nabla\boldsymbol{X} - \frac{\boldsymbol{J}}{\alpha}\right\|_F^2 \quad (11)$$

which has a closed-form solution via fast 2-D Fourier transform (FFT)

$$\boldsymbol{X}^{k+1} = \mathcal{F}^{-1}\left(\frac{\mathcal{F}\left((\boldsymbol{Y}-\boldsymbol{B}^{k+1})+\nabla^T(\alpha^k\boldsymbol{D}^{k+1}-\boldsymbol{J}^{k+1})\right)}{1+\alpha^k(\mathcal{F}(\nabla))^2}\right). \quad (12)$$

The $\boldsymbol{D}$-related subproblem is given by

$$\hat{\boldsymbol{D}} = \arg\min_{\boldsymbol{D}} \tau\|\boldsymbol{D}\|_1 + \frac{\alpha}{2}\left\|\boldsymbol{D} - \nabla\boldsymbol{X} - \frac{\boldsymbol{J}}{\alpha}\right\|_F^2 \quad (13)$$

which can be solved efficiently via a soft shrinkage operator

$$\begin{cases} \boldsymbol{D}^{k+1} = \text{shrink\_}L_1\left(\nabla\boldsymbol{X}^{k+1}+\frac{\boldsymbol{J}^k}{\alpha^k}, \frac{\tau}{\alpha^k}\right) \\ \text{shrink\_}L_1(r, \xi) = \frac{r}{|r|}*\max(r-\xi, 0). \end{cases} \quad (14)$$

Finally, the Lagrangian multipliers and penalization parameters are updated as follows:

$$J^{k+1} = J^k + \alpha^k(\nabla X^{k+1} - D^{k+1})$$
$$\alpha^{k+1} = \alpha^k \cdot \rho. \qquad (15)$$

The algorithm procedure of LRSID is summarized in Algorithm 1.

Algorithm 1 **L**ow-**R**ank **S**ingle **I**mage **D**ecomposition (**LRSID**)

Require: Degraded image Y
 1: **Initialize**:
 2: • Set parameters λ, τ_x, τ_y, α, and ρ;
 3: • Initialize $J^{(1)} = 0$, $X^{(1)} = Y$;
 4: **for** $n = 1: N$ **do**
 5:   Compute B^{k+1} by solving (6);
 6:   Solve (11) for X^{k+1};
 7:   Obtain D^{k+1} via (14);
 8:   Update J^{k+1}, α^{k+1} via (15);
 9: **end for**
Ensure: Clean Image X and B.

IV. EXTENSION TO MULTISPECTRAL IMAGE

A. Multispectral Image Low-Rank Decomposition

The LRSID destriping algorithm has utilized the spatial local smoothness in a single image. The spectral relationship is another important prior knowledge in a multispectral image cube, which could also provide extra information for better image recovery. Thus, here, we propose a Low-Rank Multispectral Image Decomposition (LRMID) model for 3-D remote sensing image cube destriping by extending the LRSID.

We generalize (4) into high-order images by replacing $\|B\|_*$ with $\sum_{r=1}^{R}\|B_r\|_*$, where $r = 1, 2, \ldots, R$, R is the total number of bands, and B_r is the stripe component matrix in the rth image of this cube. As for the image, by considering the spectral coherency, we also modify $\|X\|_{\text{TV}}$ by including the gradient along the spectral axis, as follows:

$$\|X\|_{\text{SSTV}} = \sum_i \left((\nabla_x X)_i + (\nabla_y X)_i + (\nabla_z X)_i\right) \qquad (16)$$

where $\nabla = (\nabla_x; \nabla_y; \nabla_z)$ denote the first-order forward finite-difference operators along the x-axis (horizontal direction), y-axis (vertical direction), and z-axis (spectral direction), respectively, at pixel i in the image cube. Therefore, the single-image decomposition model in (4) can be extended to a multi-image low-rank decomposition model naturally as follows:

$$\min_{X,B} \frac{1}{2}\sum_{r=1}^{R}\|X_r + B_r - Y_r\|_F^2 + \tau\|X\|_{\text{SSTV}} + \lambda\sum_{r=1}^{R}\|B_r\|_*. \qquad (17)$$

Note that, here, we still use the symbol X, B, and Y for simplicity. Here, $X = [X_1, X_2, \ldots, X_R]$, $B = [B_1, B_2, \ldots, B_R]$, $Y = [Y_1, Y_2, \ldots, Y_R]$, and $X, B, Y \in \mathbb{R}^{M \times N \times R}$. Thus, in the

multispectral image cube decomposition task, our goal is to estimate the clear image cube and the stripe cube, simultaneously.

The first term in (17) is the data fidelity term, which ensures the similarity between the desired clear image and the degraded image. The second term is the regularization term by imposing gradient-domain sparse constraints along three directions (horizontal smoothness in the spatial domain, vertical smoothness in the spatial domain, and spectral smoothness), aiming at penalizing the undesirable damage in images and preserving the sharp edges. The third term enforces the sum of the rank constraints on image bands, so that the estimated stripe component in each band is desired to be low rank. τ and λ are the regularization parameters, which control the tradeoff between the data fidelity and regularization terms.

B. Optimization

1) Stripe Update: Given image X, the stripe B can be estimated from the following minimization problem:

$$\hat{B}_r = \arg\min_{B_r} \frac{1}{2}\sum_{r=1}^{R}\|X_r + B_r - Y_r\|_F^2 + \lambda\sum_{r=1}^{R}\|B_r\|_*$$

$$= \arg\min_{B_r} \frac{1}{2}\|X_r + B_r - Y_r\|_F^2 + \lambda\|B_r\|_* \qquad (18)$$

which can be solved as (5) via the singular-value thresholding operation in (6). In fact, the stripe component is still estimated in 2-D format as the single-image case.

2) Image Update: Given stripe B, the image X can be estimated from the following minimization problem:

$$\hat{X}_r = \arg\min_{X_r} \frac{1}{2}\sum_{r=1}^{R}\|X_r + B_r - Y_r\|_F^2 + \tau\|X\|_{\text{SSTV}}. \qquad (19)$$

In the previous stripe estimation, the nuclear norm has been expressed in matrix format. While for image estimation, for the purpose of discussing numerical algorithm, we rewrite the model (19) in vector form by stacking each of them into a long column vector of size MNR $\times$ 1 according to the lexicographical order

$$\hat{X} = \arg\min_{X} \frac{1}{2}\|X + B - Y\|_2^2 + \tau_x\|\nabla_x X\|_1$$
$$+ \tau_y\|\nabla_y X\|_1 + \tau_z\|\nabla_z X\|_1. \qquad (20)$$

The difference between (7) and (20) is the extra spectral smoothness along the z-axis. Therefore, by adding an extra variable and letting

$$D = \begin{bmatrix} D_x \\ D_y \\ D_z \end{bmatrix} \quad \nabla = \begin{bmatrix} \nabla_x \\ \nabla_y \\ \nabla_z \end{bmatrix} \quad J = \begin{bmatrix} J_x \\ J_y \\ J_z \end{bmatrix} \qquad (21)$$

we can still use the previous algorithm by only replacing the 2-D FFT operator in (12) with n-D FFT and also accordingly modifying in (14) and (15). Note that, although we use the vector form to describe our method for clarity, in our

implementation, the image cube estimation was still computed in 3-D matrix format.

V. EXPERIMENTAL RESULTS AND DISCUSSION

A. Experimental Setting

Before the destriping process, the original images were coded to an 8-bit scale for display convenience. Then, the stripes with intensity [0, 255] were added into the image. Finally, for the simplicity of parameter tuning (small intensity range means small parameter range), the striped images were normalized between [0, 1]. We compared the proposed method with several state-of-the-art destriping methods, including the wavelet Fourier adaptive filter (WFAF) [10], TV [29], statistical gain estimation (SGE) [4], UTV [16], spectral–spatial adaptive hyperspectral TV (SSAHTV) [41], anisotropic spectral–spatial TV (ASSTV) [19], low-rank matrix recovery (LRMR) [21], and TV-regularized low-rank (LRTV) method [22]. The former four are based on a single image, whereas the remaining four methods are based on multiple images. Moreover, LRMR and LRTV usually need hundreds of input image bands. Therefore, we only compare our method with them on the Hyperspectral Digital Imagery Collection Experiment (HYDICE) urban data set.

In the simulated experiments, the hyperspectral image of Washington DC Mall downloaded from [42] and Moderate Resolution Imaging Spectroradiometer (MODIS) image Terra band 31 downloaded from [43] were used. The simulated images were degraded with periodical, nonperiodical, and both horizontal and vertical stripes. In real experiments, to verify the practicability and robustness of the proposed algorithm on different kinds of stripes, we selected the MODIS image Terra band 30, the Compact High Resolution Imaging Spectrometer (CHRIS) images downloaded from [44], and the HYDICE urban data set downloaded from [45]. We also test our methods on some other imaging systems with striping artifacts, including passive millimeter waves (PMMW), infrared focal plane array (IRFPA), scanning electron microscope (SEM), and charge-coupled device (CCD).

In order to give an overall evaluation of the destriping performance, several qualitative and quantitative assessments are used. The qualitative assessments include the visual inspection, the mean cross-track profile, and the power spectrum. The quantitative evaluation indexes are peak signal-to-noise ratio (PSNR) and structural similarity (SSIM) [46].

In our implementation, parameter τ_x depends on the degree of the image stripe. The image with severe stripe will prefer a larger τ_x. We empirically set $\tau_x \in [0.0001, 0.1]$, $\tau_y = 0.005$, $\lambda \in [0.001, 0.1]$, $\rho = 1.02$, and the corresponding Lagrangian parameter $\alpha \in [0.001, 0.3]$, for all the test images. Note that a number of trial and error experiments may be carried out for the best results, but it will not cost too much, since only the parameter τ_x needs to be tuned slightly. For the compared methods, we have tried our best to tune their parameters following the rules recommended by their papers to obtain the best results. For the reproduction of our research, we will publish our code online.[1]
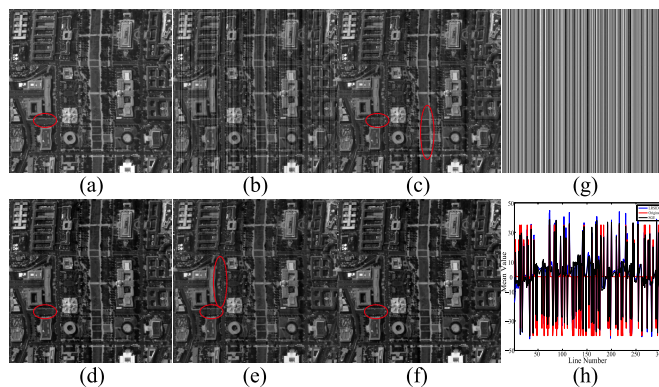
[1]http://www.escience.cn/people/changyi/index.html

Fig. 6. Simulated destriping results for the nonperiodical case. (a) Original hyperspectral image. (b) Degraded with nonperiodic stripes. Destriping results by (c) WFAF, (d) SGE, (e) UTV, and (f) LRSID. (g) Estimated stripes by LRSID. (h) Mean value comparison among the stripes estimated by LRSID, SGE, and the original one.

B. Simulated Experiments

Here, we test the proposed LRSID method on three kinds of stripe cases in a single image: nonperiodical stripes in push-broom imaging devices (representative device: hyperspectral images), periodical stripes in cross-track imaging devices (representative device: MODIS images), and both horizontal and vertical stripes (representative device: IRFPA images). In addition, we verified our LRMID destriping method on multispectral images. In our simulation, we added the synthetic additive stripe onto the original image, according to the observed model (1).

1) Nonperiodical Stripes: We performed the first simulated experiment to demonstrate the effectiveness of the proposed model in handling nonperiodical stripes. In the simulated process, the locations (part columns of the image are degraded by stripes) and the intensity value (different stripe lines are with different intensity values) of each stripe line were randomly distributed on the image. Fig. 6 displays the destriping results of various methods. It is obvious that many residual stripes are still existing in Fig. 6(c) via WFAF. In Fig. 6(d), the SGE method obtains a satisfactory result. The UTV method removes the most noticeable stripes, whereas some residual stripes still can be observed and image structures with the same direction as the stripes are also suppressed, as shown in Fig. 6(e). In Fig. 6(f), the stripes are perfectly removed without the introduction of any noticeable artifacts. The estimated stripe component by our method is shown in Fig. 6(g). For better visualization, we enhanced the contrast of the stripe component. Since SGE was designed to estimate the stripe component, we compared the estimated stripes between LRSID, SGE, and the true. As shown in Fig. 6(h), both methods obtain correct estimation at high frequencies (rapid variations) of the stripes, while still introducing some minor errors at low frequencies of the stripes. We attribute this phenomenon to the image content since this Washington DC image has many stripelike line structures, such as the vertical road and the house edge. Therefore, both methods may regard these structures as the stripe to be removed.

2) Periodical Stripes: To illustrate the effectiveness of the proposed algorithm in removing periodical stripe, we show the destriping results of different methods in Fig. 7. In this case, six stripe lines in every ten lines were periodically added into
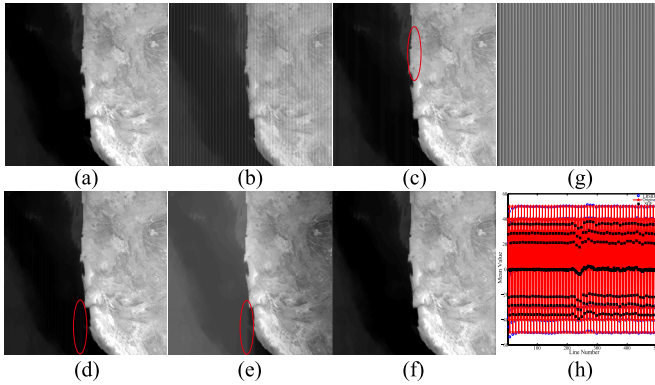
Fig. 7. Simulated destriping results for the periodical case. (a) Original MODIS image. (b) Degraded with periodic stripes. Destriping results by (c) WFAF, (d) SGE, (e) UTV, and (f) LRSID. (g) Estimated stripes by LRSID. (h) Mean value comparison among the stripes estimated by LRSID, SGE, and the original one.
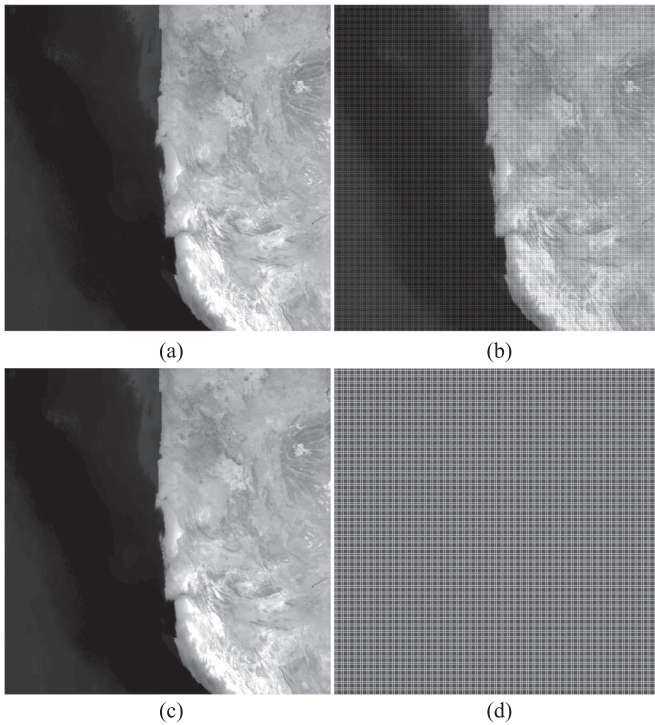

Fig. 8. Simulated destriping results for both horizontal and vertical cases. (a) Original MODIS image. (b) Degraded with both horizontal and vertical stripes. (c) Destriping results by LRSID. (d) Estimated stripes.

the stripe-free MODIS image band 31. It is worth noting that our method is totally blind to the location and periodicity of the stripes. Our LRSID still obtains the best visual performance among the compared methods. Moreover, in Fig. 7(h), our estimated stripes are almost the same as the original stripes, whereas the stripes estimated via SGE are slightly different from the true stripes. We also performed another interesting experiment on images with both horizontal and vertical stripe lines, which always exist in time-delay-integration CMOS image sensors [47]. Since some methods can only handle the stripe with one direction or may need the extra spectral information, we only show the result of our LRSID, as shown in Fig. 8. The estimated image [see Fig. 8(c)] does not contain any residual stripes, and the striped image does not contain any image structure [see Fig. 8(d)].
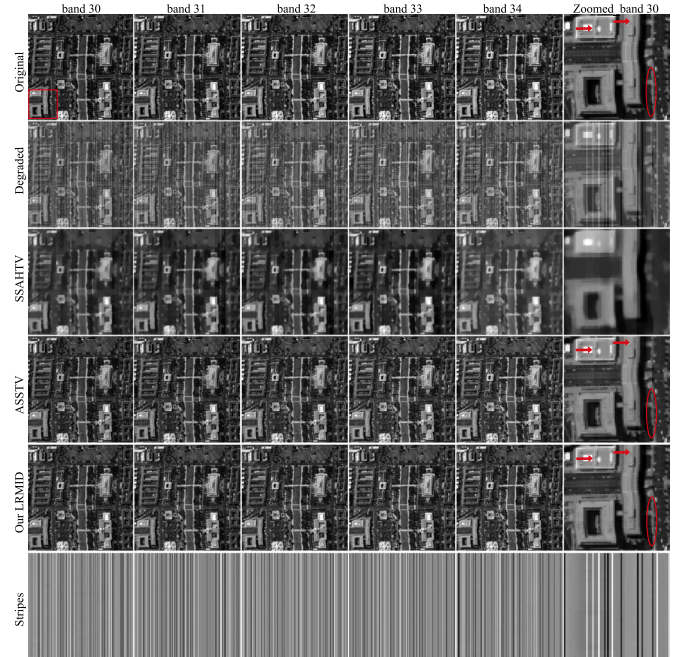

Fig. 9. Simulated destriping results for the multispectral image case. The first row shows the original hyperspectral images. The second row shows the simulated hyperspectral images with different nonperiodical stripes. The destriping results of SSAHTV, ASSTV, and our LRMID are shown from the third to fifth rows, respectively. The last row is the estimated stripes by our LRSID. The first to fifth columns show the images from band 30 to band 34. The last column shows the zoomed results for the marked red part in band 30.

From the aforementioned simulated experiments of single-image destriping, we can find that our LRSID is robust to various kinds of stripes and outperforms other methods, in terms of image structure preserving and stripe removal. This is mainly because LRSID employs the structural information TV regularization on image and the low-rank constraint on stripe, simultaneously, which demonstrate the effectiveness of the image decomposition strategy for image destriping.

3) Multispectral Image Stripes: We evaluate the proposed LRMID method on simulated multispectral striped images in Fig. 9. We randomly added the nonperiodical stripe on hyperspectral images from band 30 to band 34, and the locations of the stripes between the neighbor bands were different. From the results, we can observe that the result of SSAHTV still shows some residual stripes and an obvious oversmoothness artifact. The ASSTV method can remove most of the stripes, but it also degrades the image structures with the same direction as the stripes, as labeled by the red arrow in the zoomed image. Compared with ASSTV, LRMID utilizes the conventional TV to preserve the image structure, while UTV may easily enforce too much smoothness across the stripe. More importantly, LRMID utilizes the nuclear norm to regularize the stripe component and can significantly increase the discriminative ability for stripe component.

4) Qualitative Analysis: We further test the performance of the proposed LRSID method by two qualitative assessments: the mean cross-track profile and the power spectrum. Fig. 10 shows the mean cross-track profile of the MODIS image shown in Fig. 7 as an example. The horizontal axis stands for the column number, and the vertical axis represents the mean value of each column. We can observe some mild burrs in the curves
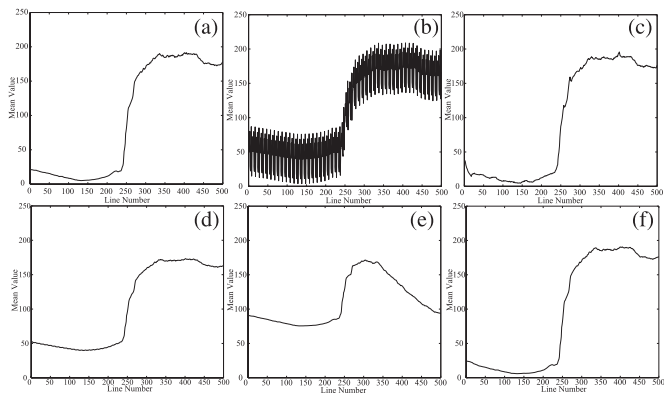
Fig. 10. Spatial mean cross-track profiles for images shown in Fig. 7. (a) Original image. (b) Striped image. Destriping results by (c) WFAF, (d) SGE, (e) UTV, and (f) LRSID.
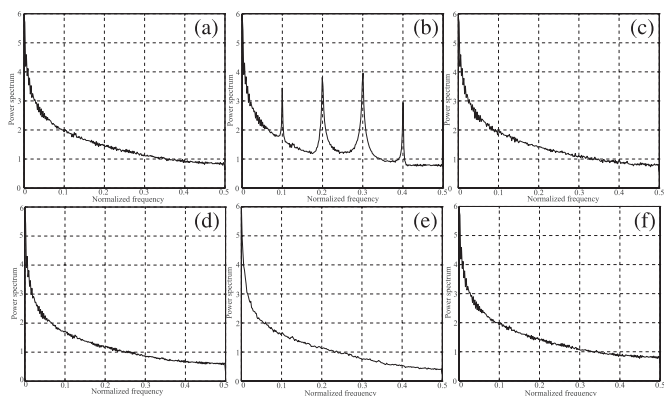

Fig. 11. Power spectrum for images shown in Fig. 7. (a) Original image. (b) Striped image. Destriping results by (c) WFAF, (d) SGE, (e) UTV, and (f) LRSID.

in Fig. 10(c) and (d), indicating that there are some residual stripes in the WFAF and SGE results. The UTV has distorted the result where a large gradient across the stripe exists. The resulting mean cross-track profile of LRSID is almost same as that of the original.

Fig. 11 shows the power spectrum of the MODIS image in Fig. 7 as an example. For better visualization, the spectral magnitudes (the y-axis) are plotted with a logarithmic scale, and the frequencies (the x-axis) are plotted with normalized frequency. In Fig. 11(b), there are several large impulses in the curve due to the effects of stripes. After destriping, our method removes all the huge large impulses, indicating that all the stripes have been removed from the image, while it has preserved almost all the small burrs, meaning that the texture and image structure are well preserved. Other methods leave unexpected impulses [see Fig. 11(c)] or oversmooth the curve [see Fig. 11(e)]. In Fig. 11(d) and (e), the power spectrum slightly shifts, due to the energy loss.

5) Quantitative Evaluation: To demonstrate the robustness of our LRSID method in the presence of different levels of stripe, the quantitative assessments, including PSNR and SSIM values, are reported in Tables I and II, respectively. In the tables, the intensity parameter means the mean absolute value of the stripe lines, and r denotes the ratio of the stripe area within the image. The highest PSNR and SSIM values are highlighted

in bold. We have the following observations. First, the SGE and proposed LRSID methods achieve the highest PSNR and SSIM values in most cases, which verify the effectiveness of the low-rank constraint for the stripes. Second, in periodical stripe cases, our LRSID has more advantages over other methods than that of the nonperiodical case since the periodical stripe meets the low-rank characteristic more. Third, with the increasing of stripe level, the advantage of our method over other methods becomes bigger. The main reason why SGE performs well in simulated experiments is that it assumes the rank-1 model for the stripe, which only meets the fact that we simulated stripe with rank 1. However, for most real remote sensing images, this assumption will be violated. We will show how our LRSID method still works in complex situations.

C. Real Experiments

Here, various real-world striping data sets were used in our experiments to demonstrate the robustness and efficiency of our algorithms.

1) Single-Image Stripe Removal: We have chosen three representative nonperiodical stripe images of push-broom-based imaging systems and three periodical stripe images of cross-track-based imaging systems, as shown in Fig. 12. The striped image selected from CHRIS band 31, as shown in Fig. 12(a), is highly contaminated by nonperiodic stripes. Fig. 12(b) shows the light nonperiodic stripe in CHRIS image band 12, wherein some obvious image structure is quite similar to the stripe. Fig. 12(c) is a subimage extracted from HYDICE image band 103, in which nonperiodical stripes exist. Fig. 12(d)–(f) shows three representative periodical stripe categories in MODIS image: detector-to-detector stripe, mirror-side stripe, and random stripe.

Figs. 13–18 show single-image destriping results. It is shown that our LRSID method has fully decoupled the stripe and image components and consistently outperforms the compared methods with the best visual quality. There are several points worth noting. First, in Fig. 15, we compare our single-image-based LRSID with multispectral image low-rank-based LRMR [see Fig. 15(e)] and LRTV [see Fig. 15(f)]. It is shown that the LRSID has removed the stripes perfectly, while there are still some residual stripes in their results, which demonstrate that the low-rank constraints on stripe are more reasonable and effective in the stripe removal issue. Second, in Fig. 16, i.e., the zoom version of Fig. 15, we can observe that our LRSID method obtains more clear image with fewer stripes and more visual smoothness appearance, due to the effectiveness of the TV term on the image. Third, in the heavy stripe case (see Figs. 13 and 15), our method can remove the stripe more completely than the others. Fourth, in both heavy (see Fig. 13) and light stripe cases (see Fig. 14), our method preserves the image structure more intactly, whereas other methods fail to achieve this important goal, as indicated by red arrows in Fig. 13 and red ellipses in Fig. 14. Last but not least, our LRSID method can work well in the presence of non-rank-1 case, as shown in Fig. 18. Overall, the results of the proposed method are consistent, for all test images, and exhibit good visual quality, with fewer artifacts than those obtained by the compared methods.

TABLE I
PSNR VALUES OF DIFFERENT METHODS UNDER VARIOUS NOISE LEVELS. THE INTENSITY DENOTES THE ABSOLUTE MEAN VALUE OF THE STRIPES. r MEANS THE STRIPE COVERING AREA WITHIN THE IMAGE

| Image | Method | Stripe Noise | | | | | | | | | | | | | | | |
| | | Intensity=10 | | | | Intensity=30 | | | | Intensity=50 | | | | Intensity=100 | | | |
		r=0.2	r=0.4	r=0.6	r=0.8	r=0.2	r=0.4	r=0.6	r=0.8	r=0.2	r=0.4	r=0.6	r=0.8	r=0.2	r=0.4	r=0.6	r=0.8
Hyperspectral Non-Periodical Image	Degrade	34.99	32.20	30.34	29.10	25.44	22.66	20.80	19.55	21.01	18.22	16.36	15.12	14.99	12.20	10.34	9.10
	SGE	**41.85**	**42.00**	**41.34**	**39.14**	**37.53**	**36.94**	**35.81**	30.37	**34.37**	**34.29**	**33.49**	**29.75**	**30.63**	**29.99**	**29.20**	24.36
	WFAF	38.81	37.02	36.61	34.39	30.70	28.65	28.20	25.65	26.66	24.42	23.97	21.34	20.88	18.50	18.04	15.39
	UTV	40.64	39.46	38.72	35.99	33.08	31.23	29.94	26.78	28.23	25.90	24.27	21.34	20.52	17.73	15.59	13.33
	LRSID	40.90	40.52	39.76	37.14	35.34	35.34	34.19	**30.88**	33.69	32.84	31.71	28.19	29.95	29.51	28.83	**25.59**
Hyperspectral Periodical Image	Degrade	35.06	32.13	30.36	29.10	25.52	22.58	20.82	19.55	21.08	18.15	16.39	15.12	15.06	12.13	10.36	9.10
	SGE	41.13	40.80	40.99	40.87	40.79	39.76	39.57	39.23	39.98	38.38	37.44	36.99	37.01	36.71	36.93	**36.46**
	WFAF	40.45	39.33	37.16	37.30	33.71	31.65	29.33	29.25	29.99	27.54	25.07	25.03	23.73	21.73	19.17	19.12
	UTV	43.54	42.32	40.95	40.19	38.40	36.68	33.20	32.27	33.37	31.97	26.66	25.66	24.29	21.88	16.83	15.48
	LRSID	**43.54**	**43.19**	**42.81**	**42.63**	**41.36**	**40.89**	**40.83**	**40.55**	**40.59**	**40.42**	**40.42**	**39.93**	**39.58**	**38.88**	**37.84**	35.96
MODIS Non-Periodical Image	Degrade	35.18	32.06	30.34	29.11	25.64	22.52	20.80	19.56	21.20	18.08	16.36	15.13	15.18	12.06	10.34	9.11
	SGE	45.55	43.95	41.70	39.68	40.00	37.29	37.09	**34.36**	37.26	36.75	35.02	32.31	34.75	31.40	31.11	27.73
	WFAF	44.85	43.01	42.23	38.99	37.37	34.86	34.12	29.82	33.18	30.56	29.78	25.40	27.27	24.59	23.92	19.42
	UTV	45.30	44.71	43.92	40.95	38.79	37.70	35.67	32.36	34.68	33.03	30.07	27.00	27.47	25.28	21.32	18.57
	LRSID	**46.36**	**45.91**	**45.25**	**41.84**	**40.52**	**40.18**	**38.54**	33.71	**36.87**	**36.63**	**34.94**	29.99	**31.90**	**30.08**	**26.12**	21.99
MODIS Periodical Image	Degrade	35.09	32.11	30.35	29.10	25.55	22.56	20.81	19.55	21.11	18.13	16.37	15.12	15.09	12.11	10.35	9.10
	SGE	**51.11**	**50.33**	49.12	48.86	48.46	48.07	47.27	47.11	47.59	46.84	45.24	45.05	44.89	43.54	40.78	36.98
	WFAF	49.19	48.60	47.65	47.47	47.15	46.15	43.29	42.91	45.32	43.75	39.59	39.47	40.98	39.46	34.78	33.98
	UTV	47.93	47.89	47.32	47.38	45.35	45.38	43.95	44.13	44.08	43.93	41.29	41.47	39.98	39.54	34.52	34.51
	LRSID	50.36	50.29	**50.22**	**50.08**	**50.01**	**50.06**	**50.21**	**50.17**	**49.79**	**49.94**	**48.85**	**48.76**	**49.39**	**49.66**	**48.34**	**48.20**

TABLE II
SSIM VALUES OF DIFFERENT METHODS UNDER VARIOUS NOISE LEVELS

| Image | Method | Stripe Noise | | | | | | | | | | | | | | | |
| | | Intensity=10 | | | | Intensity=30 | | | | Intensity=50 | | | | Intensity=100 | | | |
		r=0.2	r=0.4	r=0.6	r=0.8	r=0.2	r=0.4	r=0.6	r=0.8	r=0.2	r=0.4	r=0.6	r=0.8	r=0.2	r=0.4	r=0.6	r=0.8
Hyperspectral Non-Periodical Image	Degrade	0.970	0.941	0.908	0.890	0.830	0.699	0.603	0.550	0.697	0.500	0.395	0.333	0.480	0.230	0.160	0.102
	SGE	**0.998**	**0.998**	**0.998**	**0.997**	**0.996**	**0.996**	**0.995**	**0.987**	**0.992**	**0.991**	**0.991**	**0.986**	**0.988**	**0.987**	**0.985**	**0.964**
	WFAF	0.990	0.985	0.985	0.980	0.959	0.934	0.931	0.907	0.918	0.863	0.859	0.808	0.794	0.669	0.671	0.551
	UTV	0.996	0.994	0.993	0.989	0.982	0.969	0.955	0.926	0.944	0.896	0.843	0.764	0.756	0.559	0.428	0.287
	LRSID	0.995	0.995	0.995	0.993	0.990	0.990	0.989	0.984	0.982	0.982	0.980	0.972	0.941	0.940	0.939	0.922
Hyperspectral Periodical Image	Degrade	0.964	0.931	0.9043	0.877	0.803	0.671	0.586	0.523	0.654	0.471	0.375	0.313	0.409	0.214	0.146	0.109
	SGE	**0.996**	0.995	**0.995**	**0.995**	**0.995**	**0.994**	0.993	0.992	0.993	0.991	0.988	0.987	0.993	0.992	**0.992**	**0.992**
	WFAF	0.990	0.988	0.981	0.982	0.962	0.946	0.916	0.910	0.922	0.881	0.821	0.810	0.793	0.695	0.589	0.579
	UTV	**0.996**	0.995	0.993	0.992	0.988	0.983	0.962	0.954	0.963	0.950	0.856	0.818	0.766	0.648	0.427	0.342
	LRSID	**0.996**	**0.996**	**0.995**	**0.995**	0.994	**0.994**	**0.994**	**0.994**	**0.994**	**0.994**	**0.994**	**0.994**	**0.993**	**0.993**	0.990	0.986
MODIS Non-Periodical Image	Degrade	0.835	0.707	0.625	0.560	0.517	0.287	0.211	0.170	0.375	0.152	0.100	0.076	0.242	0.053	0.029	0.021
	SGE	0.970	0.954	0.935	0.920	0.948	0.890	0.893	0.892	0.937	0.891	**0.905**	**0.874**	**0.923**	**0.813**	**0.829**	**0.811**
	WFAF	0.966	0.953	0.941	0.912	0.879	0.853	0.810	0.773	0.812	0.780	0.718	0.684	0.694	0.648	0.581	0.549
	UTV	**0.990**	**0.986**	**0.982**	**0.973**	0.974	0.928	0.901	0.873	0.929	0.840	0.755	0.723	0.755	0.628	0.472	0.430
	LRSID	**0.990**	0.980	0.978	0.967	**0.976**	**0.959**	**0.948**	**0.902**	**0.949**	**0.927**	0.900	0.845	0.907	0.759	0.671	0.627
MODIS Periodical Image	Degrade	0.830	0.709	0.611	0.551	0.468	0.270	0.188	0.151	0.297	0.134	0.085	0.065	0.129	0.042	0.025	0.018
	SGE	0.992	0.991	0.988	0.988	0.987	0.986	0.984	0.984	0.985	0.982	0.976	0.976	0.974	0.965	0.940	0.925
	WFAF	0.993	0.991	0.988	0.988	0.985	0.979	0.956	0.964	0.974	0.961	0.916	0.935	0.936	0.915	0.841	0.915
	UTV	0.993	0.993	0.992	0.992	0.988	0.988	0.985	0.986	0.986	0.986	0.978	0.978	0.973	0.970	0.916	0.865
	LRSID	**0.994**	**0.994**	**0.994**	**0.994**	**0.994**	**0.994**	**0.994**	**0.993**	**0.993**	**0.994**	**0.991**	**0.989**	**0.993**	**0.993**	**0.990**	**0.987**
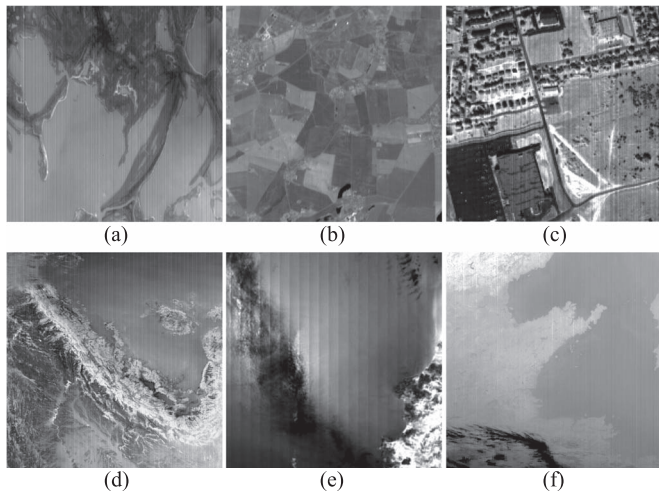
Fig. 12. Real remote sensing images. (a) CHRIS image band 31. (b) CHRIS image band 12. (c) HYDICE image band 103. (d) Detector-to-detector stripes. (e) Mirror-side stripes. (f) Random stripes.
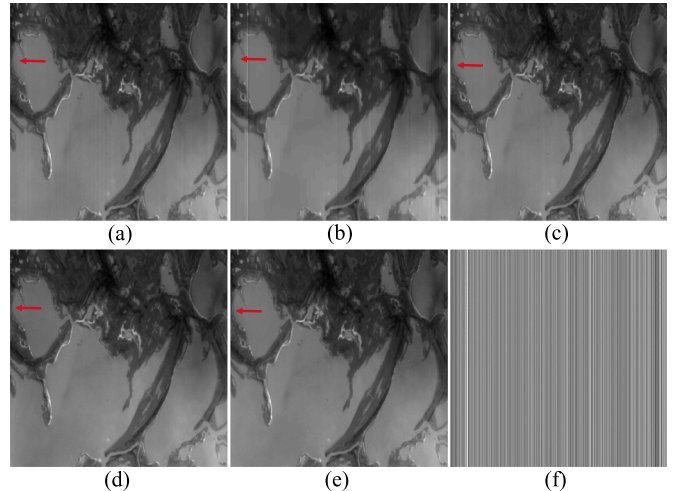

Fig. 13. Real destriping results for nonperiodical stripes in CHRIS image band 31. Destriping results by (a) WFAF, (b) TV, (c) SGE, (d) UTV, and (e) LRSID. (f) Our estimated stripes.
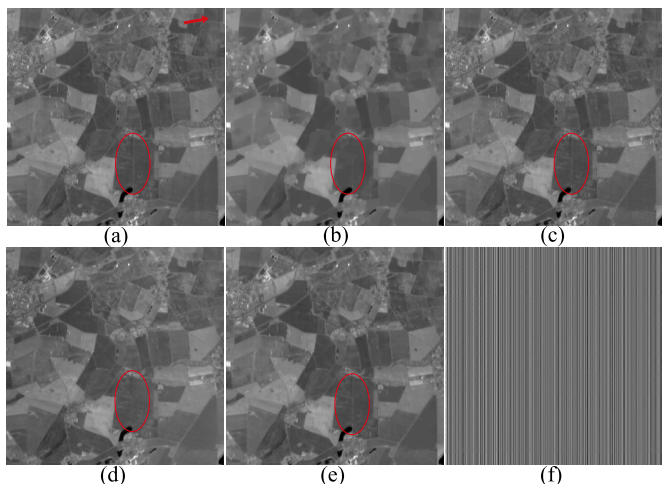
Fig. 14. Real destriping results for nonperiodical stripes in CHRIS image band 12. Destriping results by (a) WFAF, (b) TV, (c) SGE, (d) UTV, and (e) LRSID. (f) Our estimated stripes.
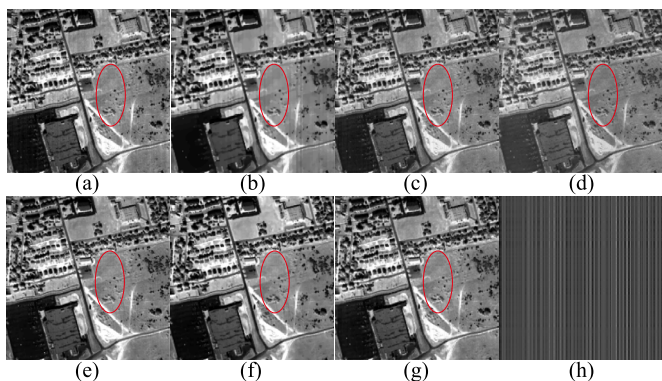

Fig. 15. Real destriping results for nonperiodical stripes in HYDICE image band 103. Destriping results by (a) WFAF, (b) TV, (c) SGE, (d) UTV, (e) LRMR, (f) LRTV, and (g) LRSID. (h) Our estimated stripes.
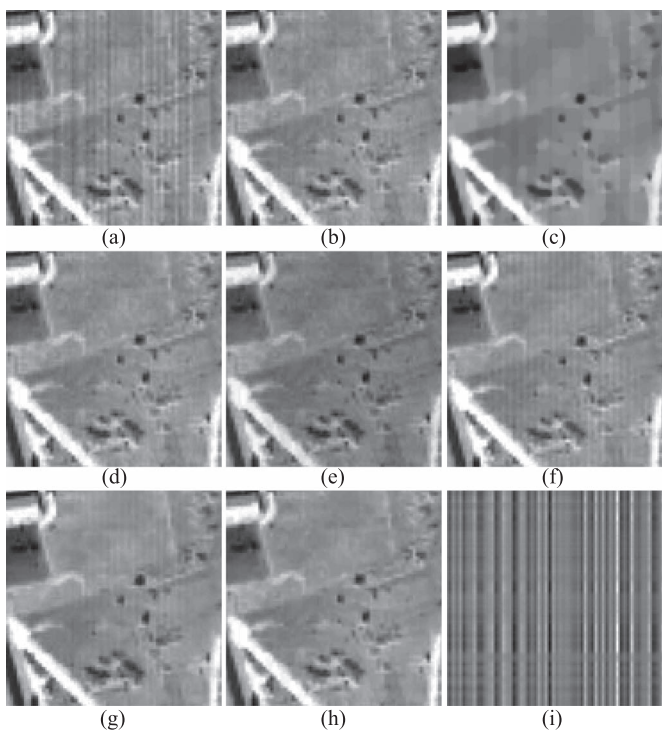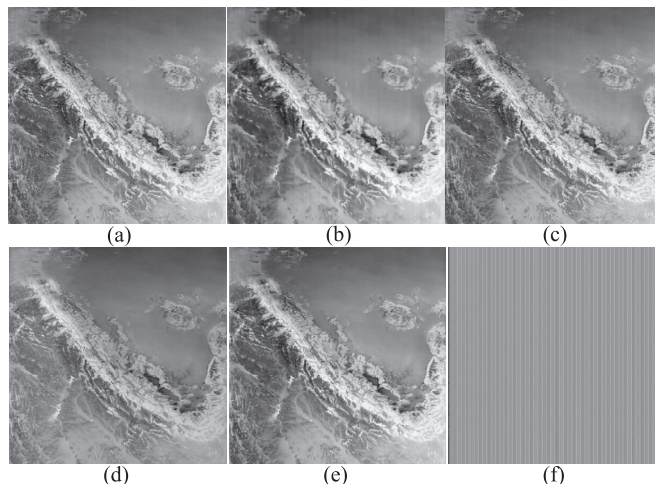

Fig. 16. Zoomed results of HYDICE image band 103. (a) Original image. Destriping results by (b) WFAF, (c) TV, (d) SGE, (e) UTV, (f) LRMR, (g) LRTV, and (h) LRSID. (i) Our estimated stripes.

Fig. 17. Real destriping results for periodical stripes in MODIS image band 30. Destriping results by (a) WFAF, (b) TV, (c) SGE, (d) UTV, and (e) LRSID. (f) Our estimated stripes.
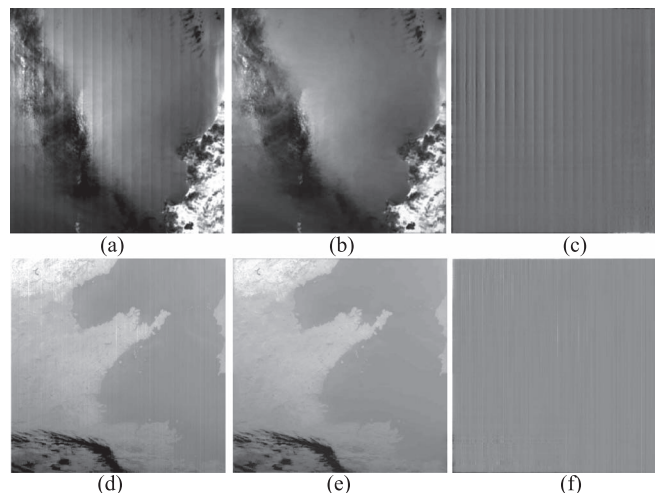

Fig. 18. Real destriping results for mirror-side stripes in MODIS image band 27 and random stripes in MODIS image band 33. Images with (a) mirror-side and (d) random stripes. (b) Estimated image and (c) stripe from (a). (e) Estimated image and (f) stripe from (d) by LRSID.

2) Multispectral Image Stripe Removal: Here, we test our LRMID method on real multispectral CHRIS images from band 32 to 37, as shown in Fig. 19. It can be clearly observed that the SSAHTV oversmooth all the images, as it is not suitable for the removal of heavy stripe. ASSTV can remove the stripe clearly, but some image structures with the same direction as the stripe are also removed. The stripes are perfectly removed by LRMID without introduction of noticeable artifacts.

3) Large-Swath Stripe Removal: Our LRSID can be also applied to real large-swath remote sensing images, such as MODIS image with $1354*2030$. In Fig. 24, we show the real destriping result for MODIS image band 27 with $1354*2030$ size. In the first row, we can observe many black holes without stripe there, indicating that the stripe component is non-rank 1. In the third row, the estimated stripe component is almost exactly the same as the stripe. This experiment demonstrates that, for real large images with non-rank-1 stripe, our LRSID method can obtain quite satisfactory results with about 2 min. Normally, for an $256*256$ image, it would cost about 3 s of running our algorithm on the personal computer with MATLAB 2014a, an Intel i7 CPU at 3.6 GHz, and 32-GB memory.
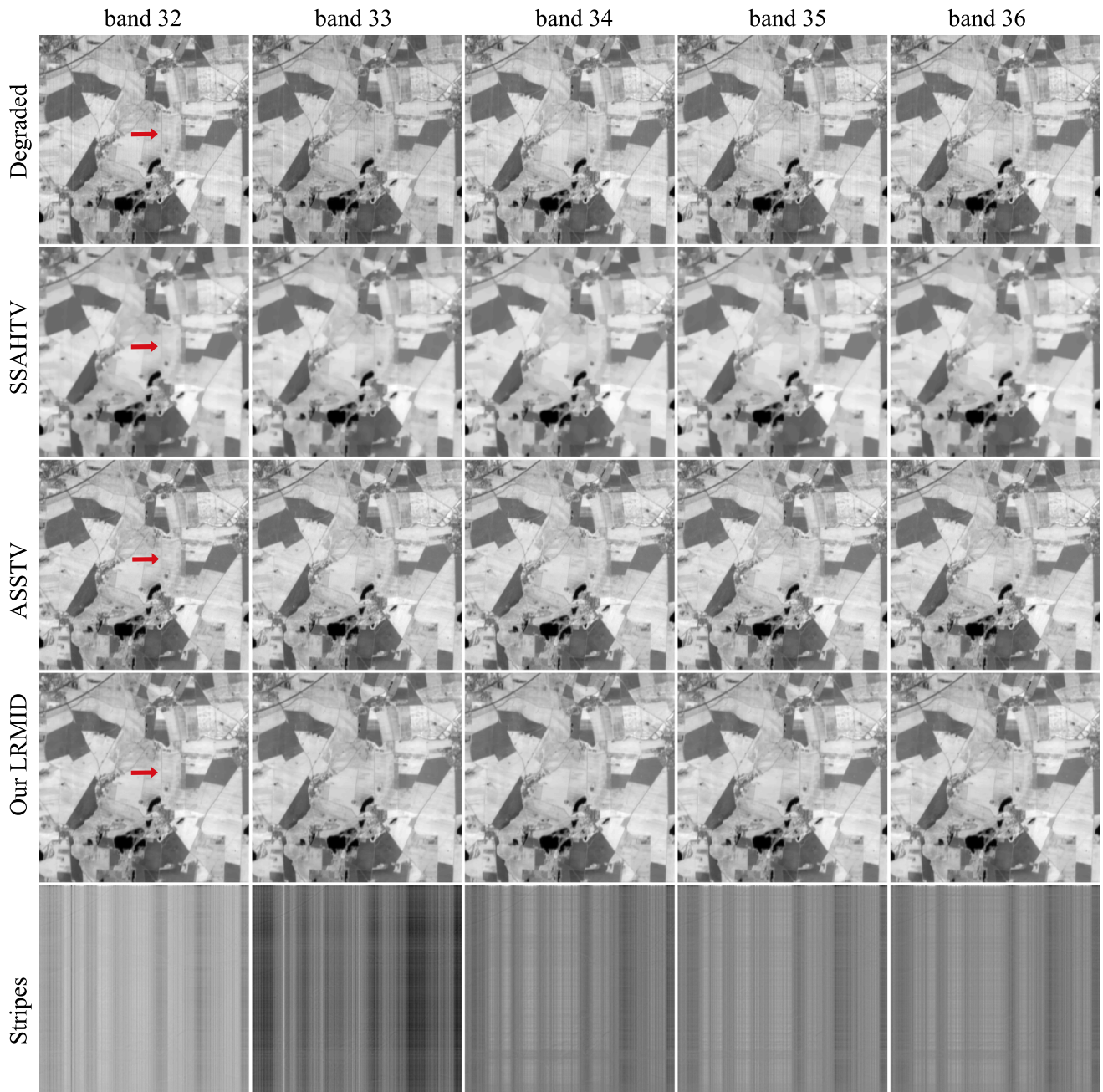
Fig. 19. Real destriping results for the multispectral image case. The first row shows the original CHRIS images from band 32 to band 36. The destriping results of SSAHTV, ASSTV, and our LRMID are shown from the second to fourth row, respectively. The last row shows the stripes that we estimated.

4) Non-Remote Sensing Images: We further test our LRSID method on various non-remote sensing images with similar striping artifacts. As shown in Fig. 20, our method shows excellent destriping performance in various striped images. Not only the estimated images are fully free from stripe issue but also the estimated stripe component is exactly belonging to its original appearance, such as vertical stripes in the PMMW image and both horizontal and vertical stripes in the IRFPA image, which strongly demonstrate the effectiveness of our method, owing to the low-rank constraint in our decomposition model. Although the stripes are much related to the particular imaging platform, our general method captures the intrinsic characteristics of the striped: directional characteristic of stripe

and its low-rank property. This is the main reason why our method works well in so many imaging systems.

5) Limitation: Although the stripe component in images is always low rank, for stripes with small fragment cases, this situation cannot be guaranteed. For example, in a MODIS Terra image band 27, as shown in Fig. 21, some obvious non-low-rank stripe fragments are left "unprocessed." An alternative is to process the striped images in a manner of small patches.

D. Interesting Extensions

Here, we apply our LRSID to some more real and practical situations but with fewer attention: multiplicative stripe and mixed random and stripe noise.
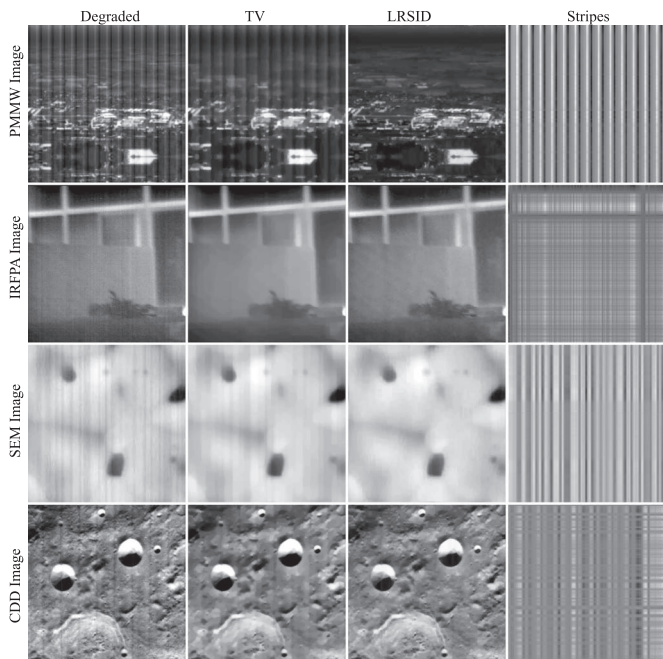
Fig. 20. Effectiveness of our method for stripes in various imaging systems. The first to the fourth row show the PMMW, IRFPA, SEM, and conventional CCD images, respectively. The first column shows the original degraded images. The destriping results of TV and our LRSID are shown from the second to third column, respectively. The last column is the estimated stripes by our method.
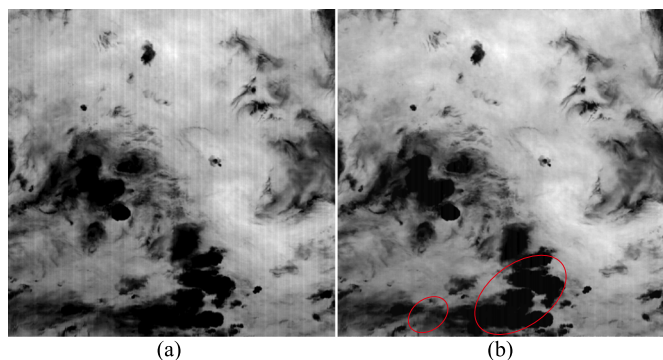

Fig. 21. Failure case of our method. (a) Original MODIS Aqua band 27 image with small fragment stripe. (b) Our LRSID result leaves the fragment stripe unprocessed.

1) Multiplicative Stripe Removal: As we have introduced in Fig. 1, for most remote sensing imaging systems, the stripes contain both additive and multiplicative components. The proposed LRSID method is designed to removed the additive stripe noise, according to the additive decomposition degraded model. However, by introducing the logarithm as in [4], our LRSID method can be used to handle the multiplicative stripe noise as well. As shown in Fig. 22(c), the multiplicative stripes have been removed satisfactorily. However, the existing works only consider additive stripe or multiplicative stripe, individually. How to blindly restore the image contaminated by both the additive and multiplicative stripes is a challenging and interesting work.

2) Single-Image Mixed Random and Stripe Noise Removal: Most destriping methods usually make use of the multiple bands to remove the mixed random and stripe noise. However, if we just have one single image or the image bands' similarity cannot be guaranteed, we have to remove the mixed noise in one single image. Our LRSID destriping method can naturally

Fig. 22. Simulated destriping result for multiplicative stripe. (a) Original image Lena. (b) Degrade by multiplicative stripe. (c) Our LRSID result.
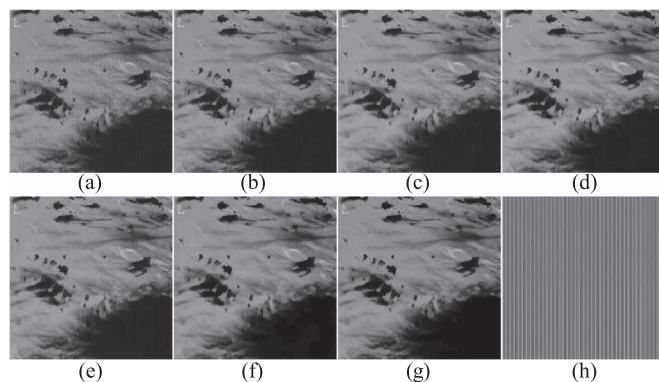

Fig. 23. Real single-image destriping result for mixed random and stripe noise. (a) Real MODIS image band 21. (b) Block-matching and 3-D filtering (BM3D) for random noise. (c) BM3D+VSNR (first denoising by BM3D [48] and then destriping via variational stationary noise remover (VSNR) [17]). (d) VSNR+BM3D. (e) WFAF+BM3D. (f) LRSID. (g) LRSID with incorporating the nonlocal image prior. (h) Stripe component.

incorporate the popular nonlocal priors [34] to further improve the restoration performance in a single image. As shown in Fig. 23(f), our LRSID can obtain a satisfactory restoration result. With incorporating the structural group sparsity prior [34] into our model [see Fig. 23(g)], the result is a more visual pleasure with smooth appearance and clear edges.

VI. CONCLUSION AND DISCUSSION

We here briefly summarize our image-decomposition-based destriping work and draw promising lines for future research in the destriping field.

A. Summary

In this paper, we proposed to remove the stripe in remote sensing images from the image decomposition perspective. Different from previous destriping works, the stripe component and image component are treated equally in our work. In this decomposition framework, the stripe and image can be estimated iteratively, in which the iterative estimation manner would benefit from each other. The low-rank prior enforced on the stripe can discriminatively distinguish the stripe from the image component, whereas the TV regularization on the image can help provide a clean image without stripe component. Moreover, via incorporating the spectral correlation in multispectral remote sensing images, we extend the decomposition model from a 2-D single image into a 3-D multispectral image case. Our methods have been tested on various simulated and real striped images, and these have achieved better destriping performance than compared methods, in terms of stripe categories, preservation of detail information, and so on.
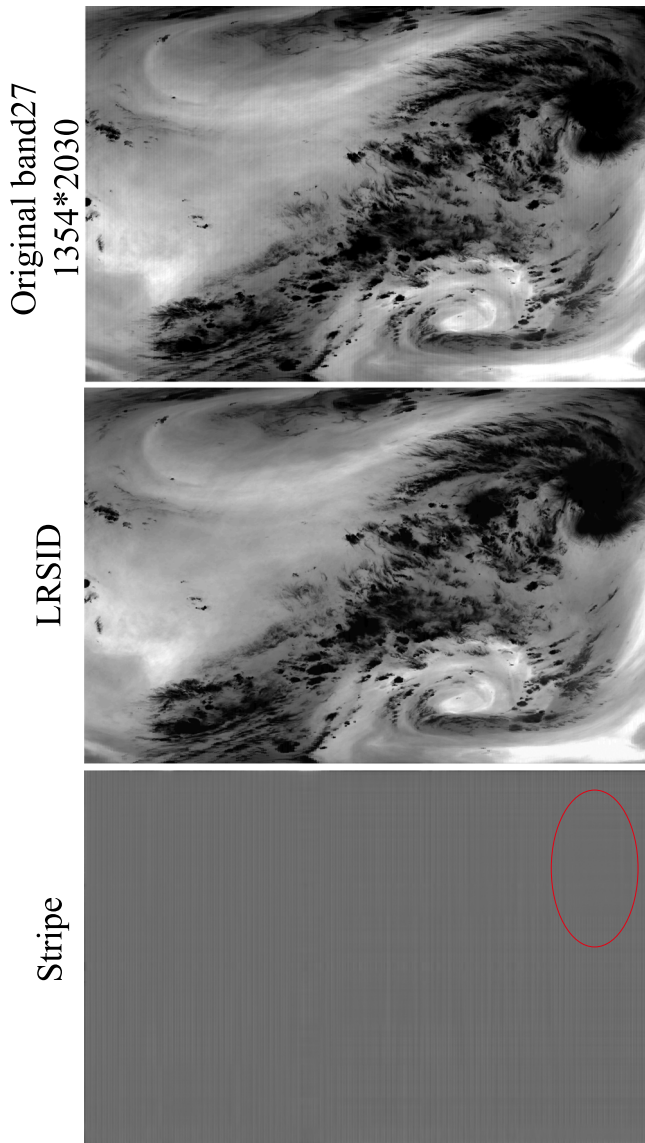
Fig. 24. Real entire swath MODIS band 27 image with 1354∗2030 size. Second row shows the estimated image component. Third row shows the estimated stripe component.

B. What Next?

1) Image Decomposition: As we have demonstrated in this work, the image decomposition strategy shows significant effectiveness for stripe removal. How to utilize more powerful tools to capture the structure characteristic of stripe is still a promising direction; for example, the directional sparsity regularization, i.e., L_{21}-norm [49], may be a good choice. Moreover, for images, the nonlocal information has shown huge success in various applications [48]. Incorporating these knowledge into our decomposition framework may further improve the final destriping performance.

2) Semiblind Image Inpainting: It is worth noting that the stripe component only influences part of the clean image. The conventional denoising methods or decomposition methods will inevitably change the value of the clean pixels. Moreover, in an inpainting way, the multiplicative stripe can also be removed without considering its degradation manner. Therefore, we believe the image inpainting methods for stripe removal

would be a promising research direction. However, unlike the conventional image inpainting, how to incorporate the domain knowledge about the stripe into the inpainting framework is an important issue. We tend to regard this stripe removal inpainting method with domain knowledge as semiblind image inpainting.

3) Deep Learning: Nowadays, with the rapid increasing of big data, including the remote sensing data, the machine learning, particularly deep learning, shows powerful ability in various applications, including image denoising, superresolution, and so on [50]. Acito *et al.* [51] have already used the subspace-learning-based dimensionality reduction technique to remove the stripes. We are glad to see more and more works via learning strategy for the development of this research area.

REFERENCES

[1] J. A. Richards and X. Jia, *Remote Sensing Digital Image Analysis: An Introduction*, 4th ed. Berlin, Germany: Springer-Verlag, 2006, pp. 343–380.

[2] H. Shen, L. Huang, L. Zhang, P. Wu, and C. Zeng, "Long-term and fine-scale satellite monitoring of the urban heat island effect by the fusion of multi-temporal and multi-sensor remote sensed data: A 26-year case study of the city of Wuhan in China," *Remote Sens. Environ.*, vol. 172, pp. 109–125, Jan. 2016.

[3] B. Koch, C. Straub, M. Dees, Y. Wang, and H. Weinacker, "Airborne laser data for stand delineation and information extraction," *Int. J. Remote Sens.*, vol. 30, no. 4, pp. 935–963, Mar. 2009.

[4] H. Carfantan and J. Idier, "Statistical linear destriping of satellite-based pushbroom-type images," *IEEE Trans. Geosci. Remote Sens.*, vol. 48, no. 4, pp. 1860–1871, Apr. 2010.

[5] P. Rakwatin, W. Takeuchi, and Y. Yasuoka, "Stripe noise reduction in MODIS data by combining histogram matching with facet filter," *IEEE Trans. Geosci. Remote Sens.*, vol. 45, no. 6, pp. 1844–1856, Jun. 2007.

[6] M.-D. Iordache, J. M. Bioucas-Dias, and A. Plaza, "Sparse unmixing of hyperspectral data," *IEEE Trans. Geosci. Remote Sens.*, vol. 49, no. 6, pp. 2014–2039, Jun. 2011.

[7] P. Ghamisi, M. Dalla Mura, and J. A. Benediktsson, "A survey on spectral-spatial classification techniques based on attribute profiles," *IEEE Trans. Geosci. Remote Sens.*, vol. 53, no. 5, pp. 2335–2353, Jun. 2015.

[8] J. Chen, Y. Shao, H. Guo, W. Wang, and B. Zhu, "Destriping CMODIS data by power filtering," *IEEE Trans. Geosci. Remote Sens.*, vol. 41, no. 9, pp. 2119–2124, Sep. 2003.

[9] B. Münch, P. Trtik, F. Marone, and M. Stampanoni, "Stripe and ring artifact removal with combined wavelet Fourier filtering," *Opt. Exp.*, vol. 17, no. 10, pp. 8567–8591, Jan. 2009.

[10] R. Pande-Chhetri and A. Abd-Elrahman, "De-striping hyperspectral imagery using wavelet transform and adaptive frequency domain filtering," *ISPRS J. Photogramm. Remote Sens.*, vol. 66, no. 5, pp. 620–636, Sep. 2011.

[11] F. Gadallah, F. Csillag, and E. Smith, "Destriping multisensor imagery with moment matching," *Int. J. Remote Sens.*, vol. 21, no. 12, pp. 2505–2511, 2000.

[12] B. K. Horn and R. J. Woodham, "Destriping LANDSAT MSS images by histogram modification," *Comput. Graph. Image Process.*, vol. 10, no. 1, pp. 69–83, 1979.

[13] M. Wegener, "Destriping multiple sensor imagery by improved histogram matching," *Int. J. Remote Sens.*, vol. 11, no. 5, pp. 859–875, 1990.

[14] P. Rakwatin, W. Takeuchi, and Y. Yasuoka, "Restoration of Aqua MODIS band 6 using histogram matching and local least squares fitting," *IEEE Trans. Geosci. Remote Sens.*, vol. 47, no. 2, pp. 613–627, Feb. 2009.

[15] H. Shen and L. Zhang, "A map-based algorithm for destriping and inpainting of remotely sensed images," *IEEE Trans. Geosci. Remote Sens.*, vol. 47, no. 5, pp. 1492–1502, May 2009.

[16] M. Bouali and S. Ladjal, "Toward optimal destriping of MODIS data using a unidirectional variational model," *IEEE Trans. Geosci. Remote Sens.*, vol. 49, no. 8, pp. 2924–2935, Aug. 2011.

[17] J. Fehrenbach, P. Weiss, and C. Lorenzo, "Variational algorithms to remove stationary noise: Applications to microscopy imaging," *IEEE Trans. Image Process.*, vol. 21, no. 10, pp. 4420–4430, Oct. 2012.

[18] Y. Chang, L. Yan, H. Fang, and H. Liu, "Simultaneous destriping and denoising for remote sensing images with unidirectional total variation and sparse representation," *IEEE Geosci. Remote Sens. Lett.*, vol. 11, no. 6, pp. 1051–1055, Jun. 2014.

[19] Y. Chang, L. Yan, H. Fang, and C. Luo, "Anisotropic spectral-spatial total variation model for multispectral remote sensing image destriping," *IEEE Trans. Image Process.*, vol. 24, no. 6, pp. 1852–1866, Jun. 2015.

[20] X. Lu, Y. Wang, and Y. Yuan, "Graph-regularized low-rank representation for destriping of hyperspectral images," *IEEE Trans. Geosci. Remote Sens.*, vol. 51, no. 7, pp. 4009–4018, Jul. 2013.

[21] H. Zhang, W. He, L. Zhang, H. Shen, and Q. Yuan, "Hyperspectral image restoration using low-rank matrix recovery," *IEEE Trans. Geosci. Remote Sens.*, vol. 52, no. 8, pp. 4729–4743, Aug. 2014.

[22] W. He, H. Zhang, L. Zhang, and H. Shen, "Total-variation-regularized low-rank matrix factorization for hyperspectral image restoration," *IEEE Trans. Geosci. Remote Sens.*, vol. 54, no. 1, pp. 178–188, Jan. 2016.

[23] W. He, H. Zhang, L. Hongyan, and H. Shen, "Hyperspectral image denoising via noise-adjusted iterative low-rank matrix approximation," *IEEE J. Sel. Topics Appl. Earth Observ. Remote Sens.*, vol. 8, no. 6, pp. 3050–3061, Jun. 2015.

[24] W. He, H. Zhang, and L. Zhang, "Sparsity-regularized robust non-negative matrix factorization for hyperspectral unmixing," *IEEE J. Sel. Topics Appl. Earth Observ. Remote Sens.*, doi: 10.1109/JSTARS.2016.2519498, to be published.

[25] X. Liu, X. Lu, H. Shen, Q. Yuan, Y. Jiao, and L. Zhang, "Stripe noise separation and removal in remote sensing images by consideration of the global sparsity and local variational properties," *IEEE Trans. Geosci. Remote Sens.*, vol. 54, no. 1, pp. 3049–3060, Jan. 2016.

[26] E. J. Candès, X. Li, Y. Ma, and J. Wright, "Robust principal component analysis?" *J. ACM*, vol. 58, no. 3, p. 11, May 2011.

[27] B. Datt, T. R. McVicar, T. G. Van Niel, D. L. Jupp, and J. S. Pearlman, "Preprocessing EO-1 Hyperion hyperspectral data to support the application of agricultural indexes," *IEEE Trans. Geosci. Remote Sens.*, vol. 41, no. 6, pp. 1246–1259, Jun. 2003.

[28] X. Xiong *et al.*, "Multiyear on-orbit calibration and performance of Terra MODIS reflective solar bands," *IEEE Trans. Geosci. Remote Sens.*, vol. 45, no. 4, pp. 879–889, Apr. 2007.

[29] L. I. Rudin, S. Osher, and E. Fatemi, "Nonlinear total variation based noise removal algorithms," *Phys. D, Nonlinear Phenom.*, vol. 60, no. 1, pp. 259–268, Nov. 1992.

[30] R. R. Schultz and R. L. Stevenson, "Extraction of high-resolution frames from video sequences," *IEEE Trans. Image Process.*, vol. 5, no. 6, pp. 996–1011, Jun. 1996.

[31] J.-F. Cai, H. Ji, C. Liu, and Z. Shen, "Framelet-based blind motion deblurring from a single image," *IEEE Trans. Image Process.*, vol. 21, no. 2, pp. 562–572, Feb. 2012.

[32] M. Elad and M. Aharon, "Image denoising via sparse and redundant representations over learned dictionaries," *IEEE Trans. Image Process.*, vol. 15, no. 12, pp. 3736–3745, Dec. 2006.

[33] J. Wright, A. Ganesh, S. Rao, Y. Peng, and Y. Ma, "Robust principal component analysis: Exact recovery of corrupted low-rank matrices via convex optimization," in *Proc. NIPS*, 2009, pp. 2080–2088.

[34] J. Mairal, F. Bach, J. Ponce, G. Sapiro, and A. Zisserman, "Non-local sparse models for image restoration," in *Proc. IEEE Conf. CVPR*, 2009, pp. 2272–2279.

[35] B. Recht, M. Fazel, and P. A. Parrilo, "Guaranteed minimum-rank solutions of linear matrix equations via nuclear norm minimization," *J. SIAM Rev.*, vol. 52, no. 3, pp. 471–501, Aug. 2010.

[36] M. Fazel, "Matrix rank minimization with applications," Ph.D. dissertation, Stanford Univ., Electrical Eng. Dept., Stanford, CA, USA, 2002.

[37] E. J. Candès and B. Recht, "Exact matrix completion via convex optimization," *Found. Comput. Math.*, vol. 9, no. 6, pp. 717–772, 2009.

[38] Z. Lin, R. Liu, and Z. Su, "Linearized alternating direction method with adaptive penalty for low-rank representation," in *Proc. NIPS*, 2011, pp. 612–620.

[39] W. Deng and W. Yin, "On the global and linear convergence of the generalized alternating direction method of multipliers," *J. Sci. Comput.*, vol. 66, no. 3, pp. 1–28, 2016.

[40] J.-F. Cai, E. J. Candès, and Z. Shen, "A singular value thresholding algorithm for matrix completion," *SIAM J. Optim.*, vol. 20, no. 4, pp. 1956–1982, Jan. 2010.

[41] Q. Yuan, L. Zhang, and H. Shen, "Hyperspectral image denoising employing a spectral-spatial adaptive total variation model," *IEEE Trans. Geosci. Remote Sens.*, vol. 50, no. 10, pp. 3660–3677, Oct. 2012.

[42] [Online]. Available: https://engineering.purdue.edu/~biehl/MultiSpec/hyperspectral.html

[43] [Online]. Available: http://ladsweb.nascom.nasa.gov/

[44] [Online]. Available: http://www.brockmann-consult.de/beam/data/products/

[45] [Online]. Available: http://www.tec.army.mil/hypercube

[46] Z. Wang, A. C. Bovik, H. R. Sheikh, and E. P. Simoncelli, "Image quality assessment: From error visibility to structural similarity," *IEEE Trans. Image Process.*, vol. 13, no. 4, pp. 600–612, Apr. 2004.

[47] Z. Liu, J. Xu, X. Wang, K. Nie, and W. Jin, "A fixed-pattern noise correction method based on gray value compensation for TDI CMOS image sensor," *Sensors*, vol. 15, no. 9, pp. 23 496–23 513, Sep. 2015.

[48] K. Dabov, A. Foi, V. Katkovnik, and K. Egiazarian, "Image denoising by sparse 3-D transform-domain collaborative filtering," *IEEE Trans. Image Process.*, vol. 16, no. 8, pp. 2080–2095, Aug. 2007.

[49] G. Liu, Z. Lin, S. Yan, J. Sun, Y. Yu, and Y. Ma, "Robust recovery of subspace structures by low-rank representation," *IEEE Trans. Pattern Anal. Mach. Intell.*, vol. 35, no. 1, pp. 171–184, Jan. 2013.

[50] H. C. Burger, C. J. Schuler, and S. Harmeling, "Image denoising: Can plain neural networks compete with BM3D?" in *Proc. IEEE Conf. CVPR*, 2012, pp. 2392–2399.

[51] N. Acito, M. Diani, and G. Corsini, "Subspace-based striping noise reduction in hyperspectral images," *IEEE Trans. Geosci. Remote Sens.*, vol. 49, no. 4, pp. 1325–1342, Apr. 2011.
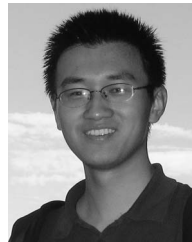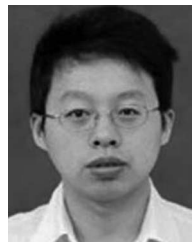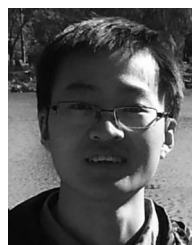
Yi Chang (S'15) received the B.S. degree in automation from the University of Electronic Science and Technology of China, Chengdu, China, in 2011 and the M.S. degree in pattern recognition and intelligent systems in 2014 from the Huazhong University of Science and Technology, Wuhan, China, where he is currently working toward the Ph.D. degree with the School of Automation.

From 2014 to 2015, he was a Research Assistant with Peking University, Beijing, China. His research interests include image processing, computer vision, and machine learning.

Luxin Yan (M'12) received the B.S. degree in electronic communication engineering and the Ph.D. degree in pattern recognition and intelligence system from the Huazhong University of Science and Technology (HUST), Wuhan, China, in 2001 and 2007, respectively.

He is currently an Assistant Professor with the School of Automation, HUST. His research interests include multispectral image processing, pattern recognition, and real-time embedded systems.

Tao Wu received the B.S. degree in biomedical engineering from the South Central University for Nationalities, Wuhan, China, in 2013. He is currently working toward the M.S. degree with the School of Automation, Huazhong University of Science and Technology, Wuhan, China.

His research interests include image processing and machine learning.

Sheng Zhong received the Ph.D. degree in pattern recognition and intelligent systems from the Huazhong University of Science and Technology, Wuhan, China, in 2005.

He is currently a Professor with the Huazhong University of Science and Technology. His research interests include pattern recognition, image processing, and real-time embedded systems.